High-throughput analysis of membrane fluidity unveils a hidden dimension in immune cell states

Luca A. Andronico[1,*], Yidan Jiang[1,2], Valentina Carannante[3], Sofia Iskrak[1], Patrick A. Sandoz[3], Jaromir Mikes[1], Andrey Klymchenko[4], Marcus Buggert[5], Anders Österborg[6,7], Björn Önfelt[3,5], Petter Brodin[1] & Erdinc Sezgin[1,*]

[1] Science for Life Laboratory, Department of Women's and Children's Health, Karolinska Institutet, 17165 Solna, Sweden.
[2] European Molecular Biology Laboratory (EMBL), 69117, Heidelberg, Germany.
[3] Science for Life Laboratory, Department of Applied Physics, KTH Royal Institute of Technology, 114 28 Stockholm, Sweden.
[4] Laboratoire de Bioimagerie et Pathologies, UMR 7021 CNRS, Université de Strasbourg 74 Route du Rhin 67401 Illkirch France
[5] Department of Medicine Huddinge, Centre for Infectious Medicine, Karolinska Institutet, 171 77, Stockholm, Sweden.
[6] Department of Hematology, Karolinska University Hospital, Stockholm, Sweden.
[7] Department of Oncology-Pathology, Karolinska Institutet, 171 77, Stockholm, Sweden.

Correspondence:

Erdinc Sezgin

erdinc.sezgin@ki.se

0046702318248

Luca Andronico

luca.andronico@ki.se

0046730653543

Abstract

Cell membranes undergo biophysical remodelling as an adaptation to the surroundings and to perform specific biological functions. However, the extent and relevance of such changes in human immune systems remain unknown, largely due to the lack of high throughput and multidimensional methodologies. Here, we describe a cytometry-based method with single-cell resolution which fills this technological gap by combining biophysical profiling with conventional biomarker analysis. This platform allows to reveal notable cell type-dependent remodelling of membrane fluidity during immune stimulations and in diseases. Using immune cells exposed to tumour microenvironment as well as from long COVID and chronic lymphocyte leukaemia patients, we demonstrate that membrane fluidity is orthogonal to surface marker expression. Moreover, this biophysical parameter identifies new functional and pathological states of immune cells previously undetected *via* surface marker profiling alone. Our findings will contribute to a more precise definition of immune cell states based on their biophysical properties and will pave the way for a better understanding of the functional heterogeneity of immune cells.

Keywords: membrane fluidity, flow cytometry, immunophenotyping, inflammation, long COVID, chronic lymphocyte leukaemia

Introduction

Immune cell heterogeneity is key for spatiotemporal control of immunity. Recent data suggests a continuum of archetypal cell states as a key component of immune system heterogeneity.[1] This concept proposes that cells can assume various states depending on their microenvironment and stimulants therein.[2] While cell types are mostly defined by surface markers or transcriptional repertoire and hence can be robustly distinguished,[3] cell state definition is more complex and indiscrete, and therefore requires multiparametric analysis.

Lipids represent a vast group of biomolecules and are highly heterogeneous in structure and function.[4] They are fundamental to maintaining cell homeostasis as they allow for energy storage *via* lipid droplets formation,[5] organelle compartmentalization, by self-organizing in membranes[6,7] and intracellular signalling by acting as secondary messengers.[8] Thus, disruption of lipid homeostasis or lipid-protein interactions leads to several diseases.[9,10,11,12] Lipids exert their function by operating as a complex dynamic system of hundreds of molecules interacting with one another. This is evident in cell membranes, where the collective interaction between different lipid species dictates properties of the membrane such as polarity, fluidity, viscosity, bending rigidity *etc*.[13,14] These biophysical properties have been shown to change during cellular processes such as proliferation and migration.[15,16,17,18,19] More recently, evidence has started highlighting the relationship between membrane biophysics and immune cell activity.[20,21,22,23,24,25,26,27,28] Importantly, alterations in cellular biophysical properties could occur without any changes in the genomic and transcriptomic profiles of dysfunctional cells (e.g., induced by nutrients or immediate microenvironment)[29,30] which makes it a complementary cell state indicator.

Cellular biophysical properties are commonly investigated by means of environment-sensitive fluorescent probes, whose photophysical properties change upon physical/chemical changes in the environment.[31,32,33,34,35] In particular, solvatochromic dyes, such as Laurdan, Nile Red and their derivatives, which shift their emission spectra as a function of local polarity and hydration, reflecting lipid order and fluidity in biomembranes are widely used.[36] However, the use of such probes remains mainly confined within microscopy techniques,[37] limiting their

application to low throughput measurements. Besides, their broad emission often prevents their use in multi-colour experiments, thereby impeding correlative analysis between biophysical properties and cell state-specific biomarkers. Here, we describe a new pipeline based on flow cytometry and a recently developed narrow-emission, plasma membrane-specific solvatochromic probe,[38] which allows for high throughput and multidimensional analysis of cell biophysical properties (Fig. 1a). After a careful optimization of the sample preparation, we measured plasma membrane (PM) fluidity from thousands of cells within a few minutes, both in healthy and patient samples. We established a multicolour panel compatible with our smart probe, and correlated PM fluidity with immune cell subtypes and functional states. Our results demonstrate how biophysical properties of cells represent an unexplored dimension in cell phenotyping and has the potential to improve our diagnostic capabilities as well as our understanding of cell (dys)functional states.

Results

Membrane fluidity can be measured at high resolution. We started by establishing an optimized flow cytometry pipeline to measure PM fluidity in a high throughput manner. We recently developed a solvatochromic probe for membrane fluidity (Pro12A),[38] which is excitable with a 405 nm laser (emission between 400-520 nm), and therefore compatible with many commercial dyes utilized for immunostaining in flow cytometry (Extended Data Fig. S1). Moreover, it is plasma membrane specific, obviating complex image processing and therefore allowing for high throughput analysis of plasma membrane fluidity. The first step in our optimization process was to assess both resolution and dynamic range of our flow cytometry setup by analysing model membranes with known fluidity. To do so, we prepared silica bead supported lipid bilayers (BSLBs) using pre-defined mixtures of lipids with different saturation degrees. BSLBs were stained with Pro12A and analysed in flow cytometry. Specifically, we collected the intensities in the blue (430-470 nm) and green (500-550 nm) regions of the emission spectrum and calculated the generalized polarization (GP)[39] (*i.e.*, an experimental readout for membrane fluidity) for individual beads. Thanks to the inherent sensitivity of Pro12A and the optimized settings (Extended Data Fig. S2), we were able to resolve minute differences in membrane fluidity and cover a wide range of membrane compositions (Extended Data Fig. S2g).[40] Given the stability and reproducibility of GP values from BSLBs over many days (Extended Data Fig. S2h), we used 1,2-Dioleoyl-sn-glycero-3-phosphocholine (DOPC)-coated beads at the beginning of each experiment on cells, to calibrate our flow setup and normalize inter-day GP measurements. Thus, we used the quantity ΔGP (defined as $|GP_{i\text{-}th} - GP_{DOPC}|$, where $GP_{i\text{-}th}$ and GP_{DOPC} represent the membrane fluidity of the *i-th* cell and the median GP of DOPC-coated beads, respectively) to compare results on membrane fluidity. Specifically, the higher the ΔGP value is, the lower the membrane fluidity is.

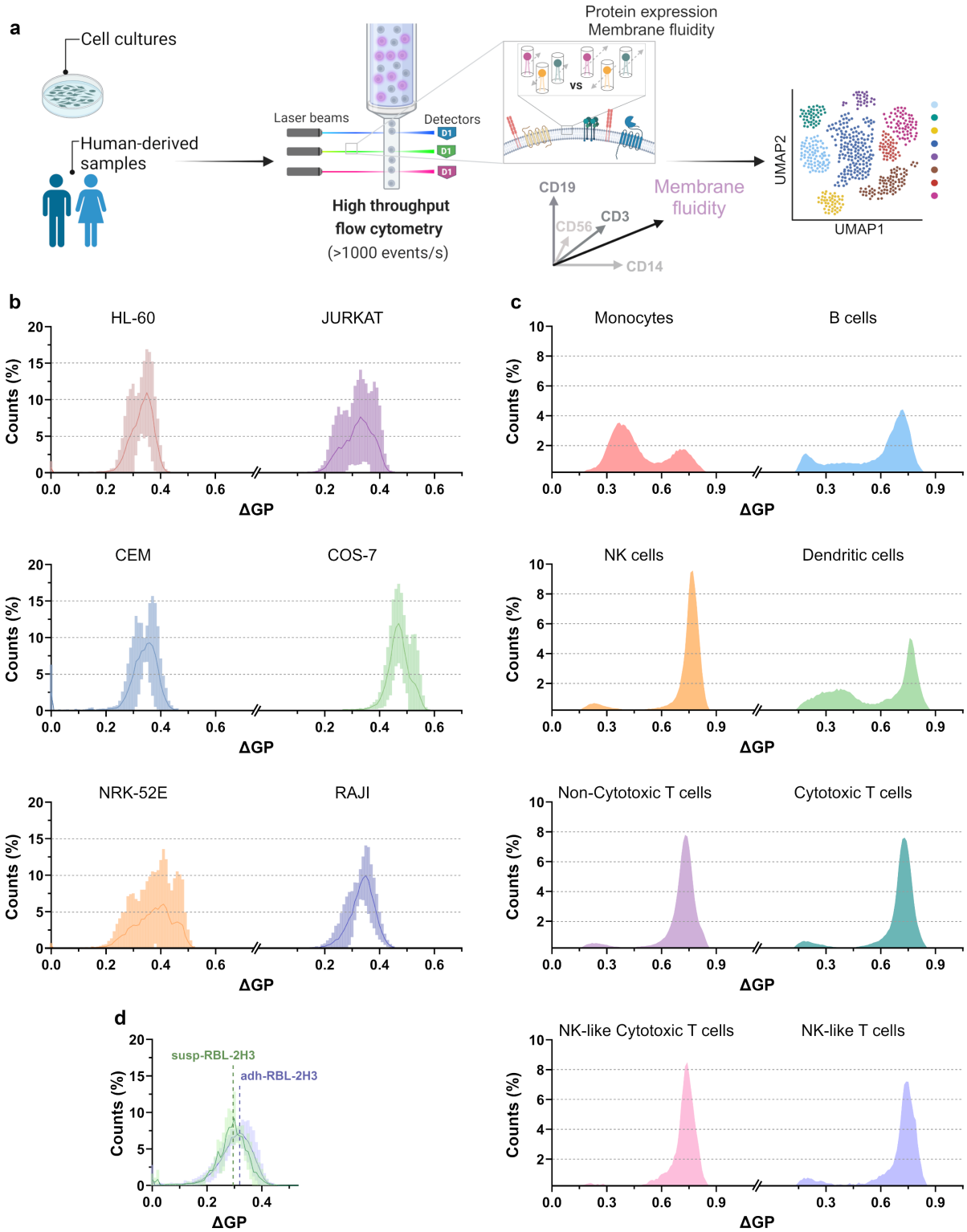

Figure 1. a, Schematic of the cytometry pipeline for high-throughput correlative analysis of PM fluidity. **b,** Histograms of ΔGP values obtained from different cell lines. The solid line shows the mean values-per-bin obtained from four independent replicates, and the bars show the corresponding standard deviation. **c,** Cumulative histograms of ΔGP values obtained from different subpopulations of Peripheral Blood Mononuclear Cells (PBMCs) isolated from healthy donors. **d,** Histograms of ΔGP values obtained from both adherent and suspension RBL-2H3 cells. The solid line shows the mean values-per-bin obtained from four independent replicates, and the bars show the corresponding standard deviation. Due to the difference in cell brightness (cell lines were much brighter than PBMCs), different optimal settings were chosen for ΔGP measurements of cell lines and PBMCs in flow. Therefore, ΔGP absolute values from cell lines should not be directly compared to those from human derived PBMCs.

Membrane fluidity is cell type specific and reveals heterogeneity. Next, we tested the compatibility of our pipeline with cell analysis. Pro12A is selective for the outer leaflet of PM but high concentrations might promote flipping to the inner leaflet and internalization.[38] To this end, we first screened different concentrations of Pro12A and staining times *via* microscopy, to identify optimal conditions for preventing internalization and cytotoxicity. By a proper titration of the dye, we were able to selectively stain the plasma membrane and prevent internalization up to ~20 minutes after staining (typical measurements of PM fluidity in flow cytometry require ~5-6 min), thus demonstrating the greater performance of Pro12A compared to other commercially available probes (Extended Data Fig. S3).[38] Lack of Pro12A internalization was also verified in our flow pipeline by analysing variations in ΔGP values over time (Extended Data Fig. S3). Indeed, following an initial stabilization time (due to the kinetic of Pro12A intercalation into the membranes), ΔGPs remained constant throughout the measurement. Furthermore, the negligible toxicity of our probe was confirmed by the unaltered ratio between the percentage of live and dead cells over time (Extended Data Fig. S3). Thus, optimized settings were used to investigate differences in PM fluidity among several cell lines (Fig. 1b). Cells showed a type-specific ΔGP average and different intra-sample variability in PM fluidity, with some cell types (*i.e.*, COS-7 and RAJI) having a narrower distribution of ΔGP values.

Our pipeline allows measuring multiple cell types at once by combining the cell surface biomarker cocktail with Pro12A. For this purpose, we measured eight different cell types simultaneously in human-derived Peripheral Blood Mononuclear Cells (PBMCs) isolated from healthy donors. Heterogeneity in membrane order (membrane fluidity is inversely proportional to lipid order of membrane) was also observed in PBMCs, which showed different PM fluidity depending on cell subpopulations (Fig. 1c). For instance, monocytes and dendritic cells (DCs) appeared to have a bimodal distribution of membrane fluidity, whereas the other subpopulations showed a small peak at ΔGP below 0.3, which refer to dead cells. The intrasample heterogeneity was also cell type-specific for PBMCs, with natural killer (NK) cells having the narrowest distribution of PM fluidity values, followed by subclasses from the T cell population.

Remarkably, our findings on cell cultures showed a systematic shift of ΔGP towards higher values (*i.e.*, lower PM fluidity) for adherent cells compared to suspension cells (Fig. 1b, d). The changes in fluidity of PM were not due to trypsinization before analysis in flow cytometry (Extended Data Fig. S4), but likely to a direct adaptation of cells to the hard extracellular environment (*i.e.*, culture plates).[41] This hypothesis is reinforced by the difference in PM fluidity observed within the same RBL-2H3 cells (basophils-like cells), when comparing the fraction of cells growing in suspension (susp-RBL-2H3) which showed higher membrane fluidity *versus* those adhering to the culture plate (adh-RBL-2H3) (Fig. 1d).

Tumours remodel membrane fluidity in innate immune cells. As we observed remodelling of PM fluidity between RBL-2H3 cells in suspension and adhering on a surface, we hypothesized that similar adaptations to the local environment could occur in multiple immune cells when they are relocated from the circulatory system to tissues. Such biophysical remodelling would be a useful marker of activation state and an orthogonal parameter to probe the microenvironment-induced functional heterogeneity. We tested this hypothesis *in vitro* by comparing biophysical remodelling of the plasma membrane in NK cells inside or outside the tumour microenvironment (TME). TME refers to an intricate network of infiltrating and resident cells, extracellular matrix, and secreted factors.[42] The accelerated metabolism of tumour cells is responsible for the generation of an acidic, hypoxic, and lipids-rich TME,[43] which contributes to reprogramming of infiltrating immune cells towards pro-tumorigenic states, and ultimately promotes and supports tumour growth. Moreover, solid tumours have material properties that can induce biophysical remodelling of immune cells therein. Thus, we investigated whether

exposure to the TME has an impact on the membrane fluidity of infiltrating NK cells. For this purpose, we grew NK cells either inside tumour spheroids grown from A498 renal carcinoma cells (iNKs) or on 2D-cultured tumour cells (2D-NKs) and compared their PM fluidity with NK cells which were cultured either outside the spheroids (oNKs) or in absence of tumour (NKs w/o tumour, Fig. 2a).[44] We calculated single-cell membrane fluidity for each condition and derived the corresponding distribution of ΔGP values for live-gated cells. As shown in Figure 2b, the presence of tumour greatly affected PM fluidity of live NK cells, causing an overall decrease in fluidity (*i.e.*, higher ΔGP) of the plasma membrane. This effect was not present in NK cells located outside the spheroids or grown in absence of tumour; however similar reduction in fluidity was observed for cells cultured on confluent 2D layers of tumour cells. A change in ΔGP was also observed when comparing the different conditions from dead-gated cells (Extended Data Fig. S5) where Pro12A internalized and stained intracellular membranes, suggesting that lipid remodelling might also affect other cellular compartments (*e.g.*, ER, mitochondria). Since the shift in ΔGPs occurred also in 2D-NKs, we concluded that the remodelling of PM fluidity might represent a direct response to the solid tumour tissue rather than an adaptation to the altered tumorigenic environment. This change in membrane fluidity could either be activating or inhibitory for the NK cell function. To address this question, we screened for expression of proteins which correlate with NKs killing activity. Specifically, we measured the levels of lysosomal-associated membrane protein-1 (CD107a, indicator of cytokine secretion)[45] and Interferon gamma (IFN-γ)[46] on all the four subsets of NK cells. As shown in Fig. 2c-d, both markers were downregulated in NK cells which have been exposed to tumour (both 2D-NKs and iNKs), suggesting a positive correlation between membrane order and NKs inhibition. Furthermore, we found that changes in ΔGP were dependent on the specific triggering stimulus. Indeed, when activated *via* Interleukin 15 (IL-15), both $CD56^{dim}$ and $CD56^{brigth}$ NK subsets showed an increase in membrane fluidity (*i.e.*, lower ΔGP) after 24h from IL-15 administration (Fig. 2e-f). This remodelling of membrane fluidity did not correlate with expression of CD56 marker, thus supporting our previous point that biophysical properties might be orthogonal to common cell surface markers and contribute uniquely to immune cell functional heterogeneity.

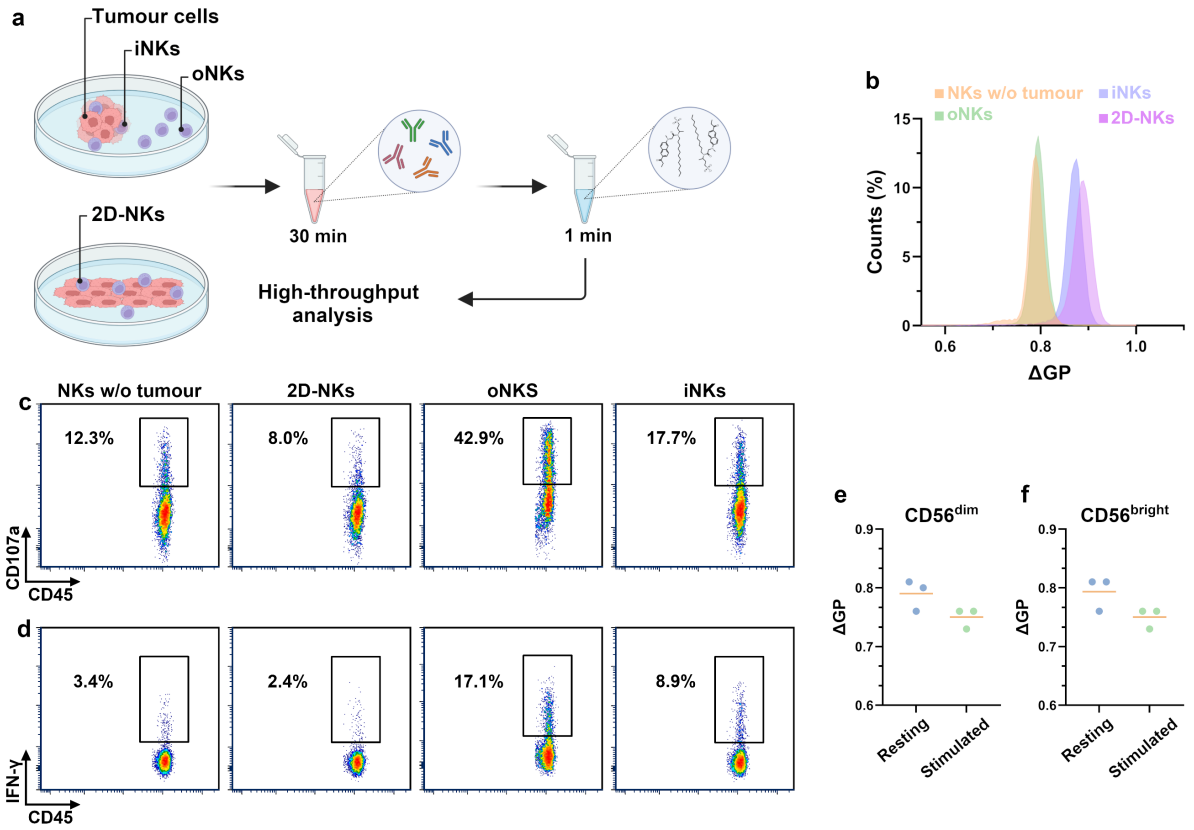

Figure 2. a, Schematic for the experiments on tumour infiltrating NK cells. **b,** Distributions of ΔGP values from the four different NK populations within live-gated cells. **c-d,** Expression of CD107a and IFN-γ markers in the four subsets of NK cells. The percentage refer to the cell number within the drawn gates. **e-f,** ΔGPs of resting (blue dots) and IL-15-stimulated (green dots) NK cells after 24 hours from IL-15 administration. Dots refer to three different healthy donors, and cells show the same ΔGP values regardless of their CD56 expression level. The plots refer to one of the four donors analysed.

Expansion of adaptive immune cells is accompanied by an increase in lipid order. As we observed changes in membrane order in activated NK cells, we asked whether similar biophysical remodelling can be used to understand functional heterogeneity in rapidly proliferating cells from the adaptive immune system. As a system to mimic the activation of immune cells, we chose γδ T cells, triggered their activation, and analysed PM fluidity during T cells expansion. Specifically, we induced *in vitro* proliferation of the $CD3^+V\gamma9^+V\delta2^+$ subset of γδ T cells (Fig. 3a) by stimulating them in PBMCs using Interleukin 2 (IL-2) and the bisphosphonate drug Zoledronate (Zol),[47] and measured PM fluidity of expanding cells over a 14-day period. Expansion of $CD3^+V\gamma9^+V\delta2^+$ cells led to a transient increase in cell size (Extended Data Fig. S6) and the formation of multiple cell populations within the $CD3^+V\gamma9^+V\delta2^+$ gate (Fig. 3a and Extended Data Fig. S6). These populations showed no differences in ΔGP within the same time-point (*e.g.*, Fig. 3a, day six), but a significant increase in membrane order was observed for all donors during expansion (Fig. 2b-e). Indeed, membrane order increased during the first six days, reached a plateau at day ten and slightly decreased at day 14. An increase in membrane order over the 14 days was also observed in the αβ T cells (*i.e.*, $CD3^+V\gamma9^-V\delta2^-$) subset, which underwent maturation to an effector state (cells showed a decrease in CD27 signal and increase in CD45RO signal, Fig. 3f and Extended Data Fig. S7). For $CD3^+V\gamma9^+V\delta2^+$-gated cells, each donor showed a rate of PM remodelling which overlapped with the rate of expansion (Figure 2g). This was not true for $CD3^+V\gamma9^-V\delta2^-$ cells, which instead did not proliferate (Extended Data Fig. S8). Interestingly,

αβ T cells showed a faster increase in ΔGP compared to γδ T cells (Fig. 3b-e). From control experiments on unstimulated γδ T cells and cells stimulated with either IL-2 or Zol (Figure. 3h-k, Extended Data Fig. S8), we concluded that remodelling of membrane fluidity might occur as a consequence of the overall activation of lymphocytes (both αβ and γδ T cells) and it is induced only by IL-2 and Zol co-stimulation. It is worth noting that PM fluidity of permeable (*i.e.*, with Pro12A internalized in intracellular environment) cells showed an opposite trend compared to PM-stained $CD3^+V\gamma9^+V\delta2^+$ (Extended Data Fig. S8), with a decrease of ΔGP values up to day ten and an inversion at day 14. This evidence supports the hypothesis that remodelling of membrane biophysical properties might also occur within the intracellular compartments, as already observed for NK cells.

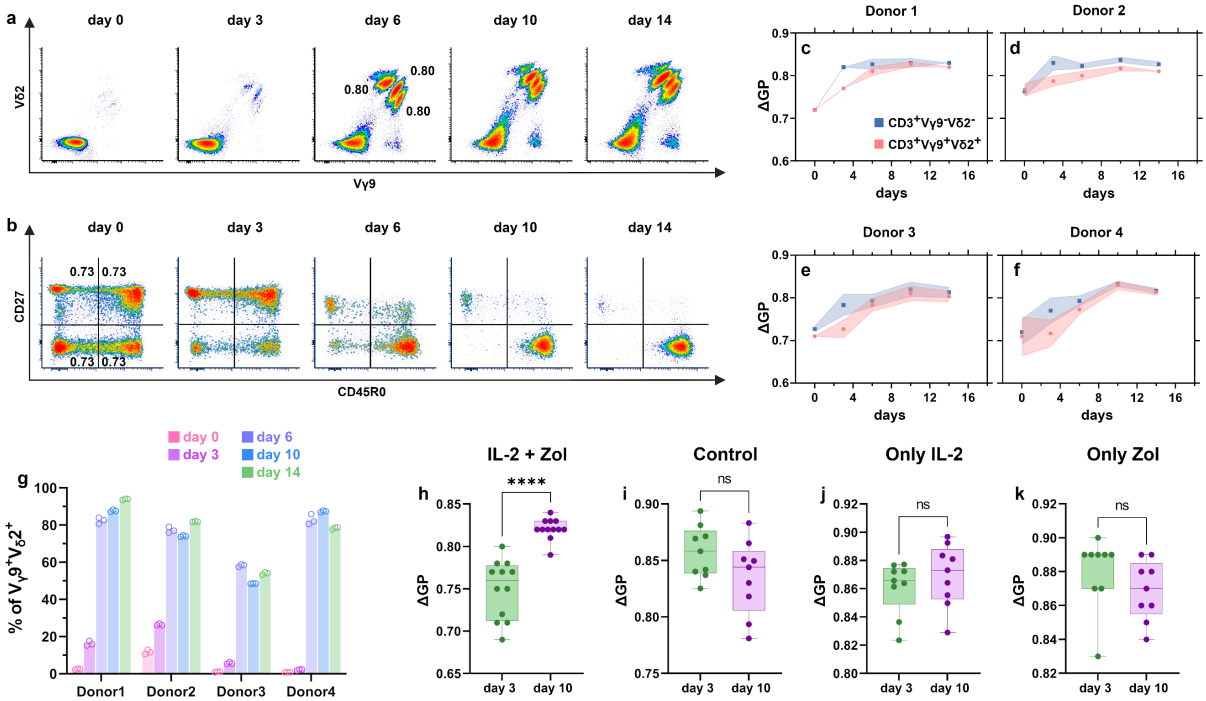

Figure 3. **a,** Expansion of $CD3^+V\gamma9^+V\delta2^+$ T cells over time, showing the occurrence of three distinct subpopulations of γδ T cells with same ΔGP (*i.e.*, 0.80). **b,** Maturation of αβ T cells ($CD3^+V\gamma9^-V\delta2^-$) over time, showing a shift in biomarkers expression from $CD27^+CD45RO^-$ to $CD27^-CD45RO^+$. The plots refer to one of the four donors analysed. **c-f,** Changes in PM fluidity (*i.e.*, ΔGP) of αβ and γδ T cells over a 14-day period after administration of Zol and IL-2. Dots per given time point refer to the median value from three technical replicates and error bands represent the corresponding standard deviations. **g,** Changes in percentage of γδ T cells over a 14-day period after administration of Zol, showing a negative correlation between the rate of expansion and the extend of ΔGP increase. Each circle refers to a different technical replicate. **h-k,** Median ΔGP values from pooled donors at day three and ten, showing difference between the control experiments and the co-stimulation of γδ T with Zol and IL-2. Statistical differences between the group at day three and ten were assessed *via* non-parametric t test using the Mann-Withney method.

Fluidity of immune cell plasma membrane discriminates health and disease states. Our *in vitro* results on NK and γδ T cells suggest that remodelling of membrane fluidity might represent a constitutive feature of activating immune cells, regardless of the type of immune response involved (*i.e.*, innate versus adaptive). Hence, membrane fluidity can be a confounding factor for immune cell functional heterogeneity. As such, alterations in membrane order of immune cells could determine the immune cells response, such as pro- and anti-inflammatory. Indeed, it has already been shown that in a healthy physiological state, disturbances in the biophysical properties of cells are corrected by compensatory mechanisms. This reinforces the hypothesis that biophysical properties of the membranes reflect cellular fitness (*i.e.*, health) and uncorrected biophysical changes might correlate with

diseases.[48] Therefore, we investigated the PM fluidity in two pathological conditions where the immune system is heavily compromised: Chronic Lymphocytic Leukemia (CLL) and Post-Acute Sequelae of COVID-19 infection (Long COVID). We first established a multicolour panel compatible with our flow cytometry pipeline and analysed human-derived PBMCs (Fig. 4a). Thus, we incubated PBMCs from healthy donors and patients with a panel of antibodies targeting the main immune cell types and gated on eight different subpopulations (Fig. 4b and Extended Data Figs. S9-11): cytotoxic T cells, non-cytotoxic T cells (mostly consisting of Helper T cells), NK-like T cells, NK-like cytotoxic T cells, B cells, monocytes (comprising both $CD11c^{dim}$ and $CD11c^{bright}$ cells), NK cells and DCs. Then, we stained antibody-conjugated cells with our probe (Pro12A) and analysed the PM fluidity of each subclass simultaneously.

We observed that staining with Pro12A probe yielded three distinct peaks of ΔGP values in different cell types (Fig. 4c and Extended Data Fig. S12). First peak (ΔGP~0.7) referred to live cells where only the outer leaflet is stained (Pro12A selectively stains the outer leaflet of PM).[38] The second peak (ΔGP~0.4) generated from live cells where Pro12A is presumably flipped to the inner leaflet, which is more fluid than the outer one,[14] due to an increased permeability of the outer leaflet. The last peak (ΔGP~0.2) referred to dead permeabilized cells where internal organelles were also stained, which are significantly more fluid than PM.[49] Microscopy images supported this hypothesis, showing the existence of three different populations among monocytes from healthy PBMCs (Extended Data Fig. S13). Specifically, we observed a clear distinction between healthy (high ΔGP and signal only from membrane) and dead (signal also from the intracellular environment) cells, whereas for the low ΔGP population, we observed the presence of PM regions with lower fluidity. All three peaks were very informative on the biophysical remodelling of different cell types in CLL and Long COVID patients. As shown in Figure 4d-k, for both CLL and Long COVID patients, PM fluidity of all cell types except B-cells (Fig. 4f) was decreased (*i.e.*, higher ΔGP) compared to healthy donors. For Long COVID patients, this overall decrease in PM fluidity could be ascribed to the systemic increase in dyhydrosphingosine and sphingomyelin concentration (sphingolipids are known to decrease membrane fluidity) observed in patients who contracted COVID-19.[50,51] In fact, a shift in lipid homeostasis during the acute phase (promoting the biosynthesis of sphingolipids) might induce a more permanent remodelling of the PM lipid composition in immune cells, which appears during the infection sequelae. Similarly, researchers have identified the expression of the Arylsulfatase D (ARSD) gene (involved in sphingolipids metabolism) in $CD19^{+}$ leukemic cells as a potential predictor of CLL progression.[52] Over-expression of the ARSD gene might also extend to other immune cell types, thus causing a corresponding remodelling of the PM biophysics. Interestingly, only monocytes and DCs showed a considerable fraction of cells within the low ΔGP range (Fig. 4g, k) for both healthy and diseased cells. Furthermore, monocytes and DCs from patients presented a right-shift (*i.e.*, lower PM fluidity) for both low ΔGP- and high ΔGP-range peaks compared to healthy donors, which suggests that a more constitutive remodelling of lipid composition might occur in CLL and Long COVID patients. Notably, NK cells, DCs and non-cytotoxic T cells from CLL patients showed a bimodal distribution centred at ~0.8 ΔGP (*i.e.*, suggesting higher heterogeneity in the fluidity of the PM outer leaflet) with relative abundances of the two local peaks which was cell type-specific (Fig. 4i-k). For some populations, we observed a small fraction of cells with ΔGP ~0.2, which refers to cells that died between the washing of viability dye and the flow analysis. These cells would be normally mis-gated as live cells; instead, the use of Pro12A allowed for their identification and separation from healthy cells. It is worth noticing that the fraction of DCs in patients who showed increased PM permeability (ΔGP distribution centred at ~0.4) correlated with increased expression of CD11c biomarker. This was true for CLL patients but not for healthy donors (Extended Data Fig. S13). This evidence reinforces once more how PM fluidity

represents an orthogonal parameter that allows the detection of cellular states which involve remodelling of membrane biophysics without necessarily affecting protein expression.

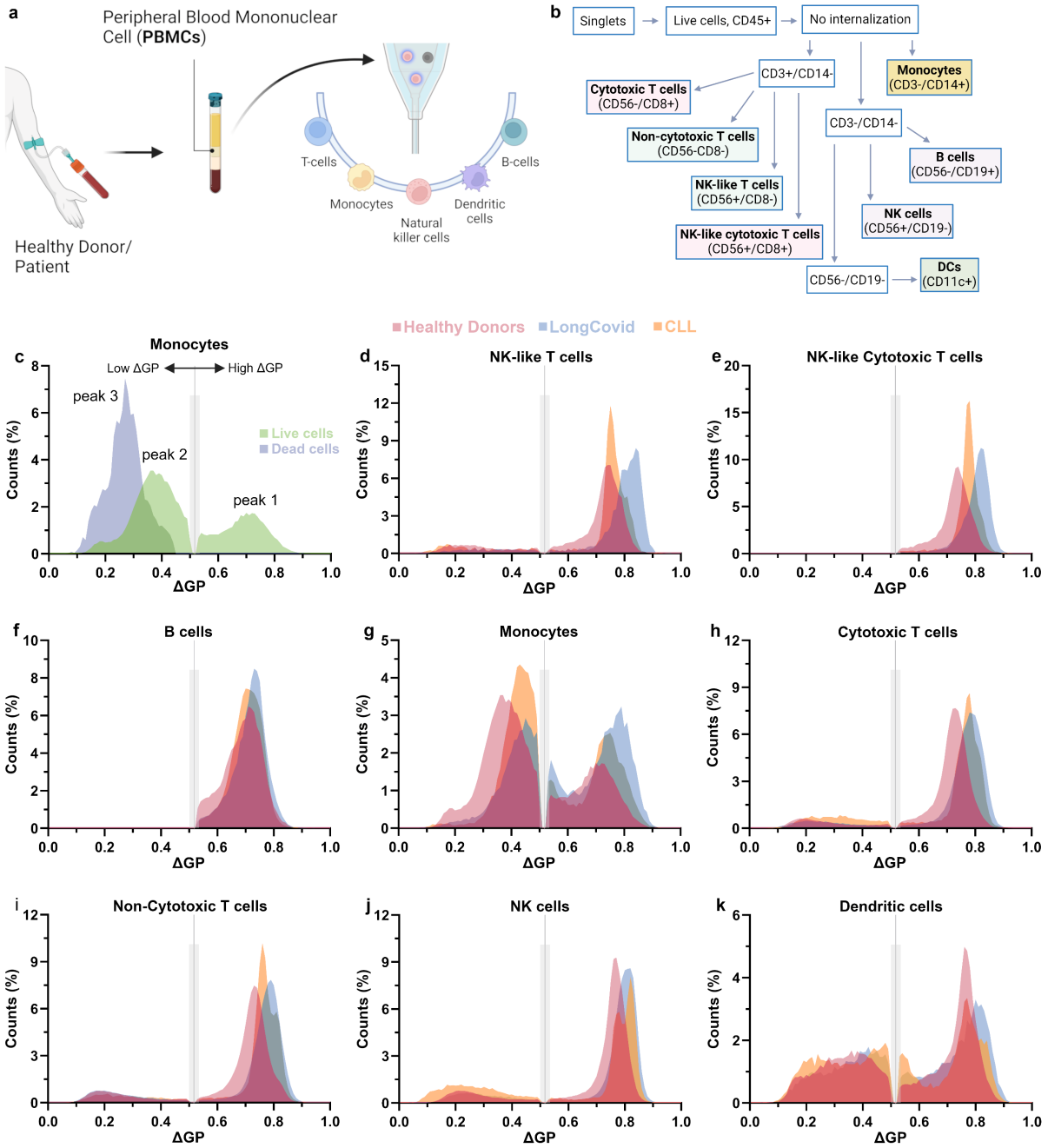

Figure 3. a, Schematic for the isolation of PBMCs from healthy donors and patients. **b,** Gating strategy to identify main subpopulations of PBMCs. **c-k,** Cumulative histograms (~10^6 cells in each histogram) of ΔGP values from immune cell subpopulations isolated from healthy donors and patients. The grey bar divides each histogram into two parts: cells with low (left side) or high (right side) ΔGP values. For plots d-k, the colour scheme follows the legend in panel d. Panel c shows data from healthy donors' samples.

PM fluidity reveals hidden cell populations. Results on human-derived PBMCs described overall changes in PM fluidity between healthy donors and patients. Furthermore, for some cell types (*i.e.*, monocytes, DCs) they showed the existence of two different pools of cells with high or low ΔGP values, which presumably refer to cells where Pro12A localizes to either the outer membrane leaflet, or scrambled in both leaflets, respectively. However, from the ΔGP histograms, it appears clear how the transition between the two groups is not abrupt but rather

a continuum. Moreover, for certain cases biophysical differences were independent of surface marker expression. These observations suggest that biophysical properties can be used as a new parameter to resolve cell states. To test this hypothesis directly, we performed Uniform Manifold Approximation and Projection (UMAP) analysis. UMAP helped us to assess whether the introduction of PM fluidity as a new dimension allows for the identification of those transitioning populations, and whether these populations present different phenotypes. Thus, we compared UMAP projections with or without ΔGP as an additional parameter, both on healthy donors and patients. For some cell types, introducing PM fluidity allowed the revealing of hidden populations, as for the case of DCs from healthy donors and monocytes from CLL patients (Fig. 5a and Extended Data Fig. S14). As shown in Fig 5a, the use of ΔGP in the UMAP analysis led to the formation of two new clusters characterized by lower ΔGP. The two new populations differed from the rest in biomarker expression (Extended Data Fig. S14), being slightly positive for CD14 and showing low expression of CD11c. Thus, based on lipid order of PM we identified new cell populations characterized by a lower membrane fluidity.

For a given cell subtype, the UMAP analysis yielded multiple clusters. This was true for both cells pooled from low ΔGP- or high ΔGP-range, and it reflects the heterogeneity in protein expression and membrane fluidity within the same immune cell type. When comparing low ΔGP-gated *versus* high ΔGP-gated cells within the same immune cell type, we observed similar UMAP projections (Fig. 5b and Extended Data Fig. S15-17), which suggests that internalization of Pro12A occurs to some extent across all cells. However, the relative cluster abundance was different between gated cells (Fig. 5b-c). Specifically, high ΔGP-gated cells with relatively low lipid order underwent greater internalization of Pro12A (*i.e.*, ΔGP=0.76 population in the high ΔGP pool has a significantly smaller number of cells in the low ΔGP pool compared to ΔGP=0.63 population). This suggests a positive correlation between fluidity of the outer leaflet and membrane permeability. Interestingly, cells with the lowest PM fluidity of the outer leaflet did not necessarily have the lowest fluidity for the inner leaflet as well (*i.e.*, median ΔGP in the UMAP projection from low ΔGP-gated cells). This evidence suggests that the biophysical remodelling of the two leaflets might be independent of one another, and therefore might play a different role in regulating cellular functions. In summary, Pro12A gives multiple orthogonal biophysical parameters for immune cell subsets in addition to biomarker expression.

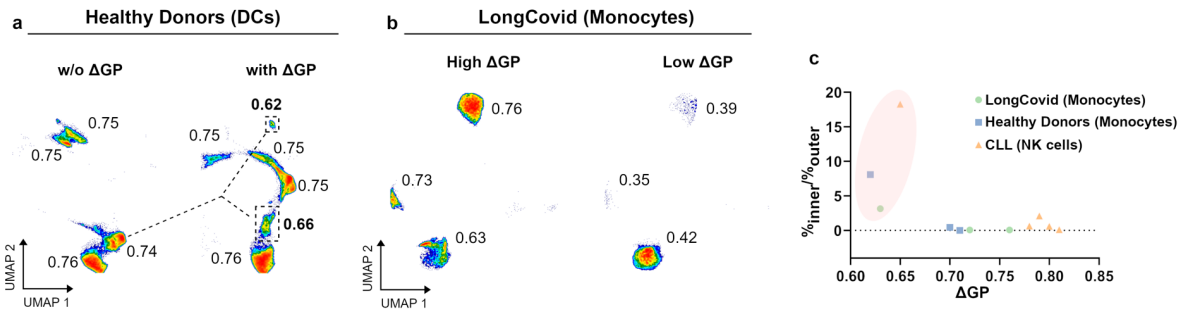

Figure 5. a, UMAP projections of DCs from healthy donors without (left) or with (right) ΔGP as additional parameter. Dashed black lines connect clusters of the same cells **b,** UMAP projections of Monocytes from Long COVID patients, showing the clustering of cells with Pro12A localized either in the outer (left panels) or inner (right panels) leaflet of the PM. Text in plot a and b refer to the clusters' median ΔGP. **c,** Plot showing the increase in Pro12A internalization as a function of ΔGP. The y-axis is calculated for each pair of clusters (with Pro12A in the inner *vs* outer leaflet) by dividing the corresponding relative abundance. Each point refers to a different cluster identified in the UMAP projections from Monocytes (healthy donors and Long COVID patients) and NK cells (CLL patients).

Discussion

Remodelling of biophysical properties of immune cells (*e.g.*, plasma membrane fluidity) occurs to ensure survival and optimal cell function during environmental changes. Here, we described a new pipeline for the measurement of plasma membrane fluidity, combining the use of environment-reporting probes with the high-throughput and single-cell multi-parameter capability of flow cytometry. From the analysis of cell cultures, we showed that PM fluidity is highly heterogeneous already under homeostatic conditions, and each cell type presents a distribution of fluidity values with a characteristic width (*i.e.*, intra-sample heterogeneity) and centre. As we observed from *in vitro* studies on NK and γδ T cells, PM order also changes during immune response and in a stimulus-dependent manner. This evidence strongly highlights the importance of investigating PM fluidity remodelling as a means of cell adaptation/response to the environment. For instance, by modifying membrane order, immune cells might increase their survival within the TME, enhance their migratory capacity[17] and effector activity. Indeed, it has been shown that PM fluidity influences immune synapses integrity[53] and, therefore, might play a key role in overall immune responsiveness. While in some cases, PM remodelling might derive from alterations in just one or few well-defined signalling pathways (as in the instance of using drugs or stimulating agents) for tumour infiltrating cells, changes in PM fluidity might generate as the result of multiple converging processes triggered by both physical stresses (*e.g.*, increased in local pressure or smaller cell confinement) and biological stimuli (*e.g.*, altered metabolism in the TME). Thus, measuring the fluidity of the plasma membrane could be a straightforward approach to detect pathological states in cells, allowing diagnostic sensitivity without the need to delve into the underlying complexity of the system under examination. Following this rationale, we explored the possibility of using this property as a discriminant between health and diseases and analysed the membrane fluidity of the main subpopulations of PBMCs isolated from CLL and Long COVID patients. Our findings showed clear differences between cells from healthy donors and patients, which could result from the aberrant lipid metabolism and dyslipidaemia observed in both conditions. However, while most studies on both diseases described an imbalance in lipid homeostasis at a systemic level, using our flow pipeline we were able to retain single-cell resolution and analyse multiple cell types at once. We showed how different subsets of immune cells undergo a different remodelling of PM fluidity, although being exposed to the same systemic alterations. Therefore, the study of PM fluidity by solvatochromic probes has the potential to bring new insights into inflammatory mechanisms that are triggered by factors such as defined pathogenic insults or even dietary habits that might have a direct effect on cellular biophysics. Our flow pipeline is highly versatile in multiplex capability and scope (*e.g.*, several biophysical properties of intracellular membranes can also be investigated by means of smart probes which target subcellular organelles or report on different properties like membrane viscosity, tension *etc.*)[54] and it can be easily integrated with any commercial flow cytometer. Remodelling of cell biophysics continues to gain attention as an active player in defining health and diseases, and the present work represents the first effort towards establishing PM fluidity as a new parameter orthogonal to classical multi-omics analysis in molecular biology and bringing cell biophysics into biomedical practises.

Methods

Synthesis of BSLBs with different membrane fluidity. Silica beads and lipid species (Cholesterol, 1,2-dioleoyl-sn-glycero-3-phosphocholine (DOPC), 1-palmitoyl-2-oleoyl-glycero-3-phosphocholine (POPC) and 1,2-dipalmitoyl-sn-glycero-3-phosphocholine (DPPC)) were purchased from Bangs Laboratories and Avanti Polar Lipids, respectively. Synthesis of BSLBs

consisted of two steps: *i)* formation of liposomes with given PM fluidity and *ii)* coating of silica beads with a specific liposome composition. *Formation of liposomes*. For each lipid species, 10 µL of lipid solution in Chloroform (25 mg/mL) was transferred to a 1.5 mL Eppendorf and dried out under a Nitrogen flow. Then, 1 mL of *ad-hoc* buffer (SLB buffer: 10 mM HEPES, 150 mM NaCl, pH=7.4) was added to hydrate the lipid layer for 5 minutes under vigorous vortexing, and the solution was sonicated for 10 minutes (tip sonication, power=3, duty cycle=40%) to yield ~30 nm-sized liposomes. *Coating of silica beads*. 5 µm-sized beads were washed 2x with SLB buffer, resuspended in 45 µL of liposomes solution and diluted to 500 µL final volume in SLB buffer. Complete coating of silica beads was achieved after 30 minutes in bath sonication, after which beads were washed 2x in SLB buffer to remove excess of liposomes and stored a +4 ˚C.

Pro12A internalization and cytotoxicity. Synthesis of Pro12A was reported previously.[38] We assessed degree of internalization and cytotoxicity of Pro12A by acquiring images in spectral confocal microscopy (LSM780 Zeiss microscope) over time and at different concentrations. Dye was considered internalized and cytotoxic when signal from the intracellular environment became visible or blebbing of the plasma membrane started occurring, respectively (Extended Data Fig. S3). 8-wells ibidi chambers were precoated with BSA (3 mg/mL) for 30 minutes and 100 µL of CEM cells ($6x10^6$ cells/mL in Leibovizt (L-15) medium) were added to each well and topped up with additional 300 µL of fresh L-15 medium. To each well, 1 µL of Pro12A was added to a final concentration of either 0.25 µM or 2.25 µM, and t-stack images were acquired (10 images every 90 seconds). Cell-specific membrane fluidity was calculated using a customized software written in Python.

Optimising resolution for PM fluidity measurements. We prepared BLSBs with either low (DPPC-Cholesterol 1:1 coated beads) or high (DOPC coated beads) membrane fluidity and used them to identify the best PMT voltages in the blue and green channels of the flow cytometer (BD LSRFortessa). 50 µL of liposomes-coated beads was diluted into 500 µL of SLB buffer and stained with 1.5 µL of Pro12A under vortexing. Acquisition of flow data started after 1 minute from dye addition. From the theoretical map of ΔGPs *vs* amplification factors (Extended Data Fig. S2), we selected two different areas of low and high intensity signals and performed a voltration in one channel while keeping the PMT in the other channel constant. By doing so, we were able to identify the optimal pair of PMT voltages which ensured the highest resolution (*i.e.*, largest ΔGP between low and high fluidity membranes) and reproducibility of GP measurements.

Cell cultures. Suspension cells (CEM, HL60, JURKAT, RAJI and RBL) were cultured in RPMI-1640 medium supplemented with 10% foetal bovine serum (FBS, Sigma Aldrich) whereas adherent cells (COS7 and NRK) were cultured in DMEM medium supplemented with 10% FBS. Cells were cultured at a density of 10^6 cells/mL (suspension cells) or at >70% confluency (adherent cells) at 37 °C and 5% CO_2.

NK cell isolation and activation. NK cells were obtained from anonymous buffy coats (Karolinska Hospital, Huddinge, Sweden) by negative selection using EasySep Direct Human NK cell isolation kit (Stemcell Technology) according to manufacturer's instructions. Isolated NK cells were maintained in RPMI-1640 with L-glutamine (Sigma-Aldrich) supplemented with 10% FBS, 1x MEM Non-Essential Amino Acid Solution (Sigma-Aldrich) and 10 mM Hepes (Sigma-Aldrich). NK cells were incubated overnight with IL-15 (R&D System) at final concentration of 10 ng/mL (IL-15 activated NK cells) or in the absence of IL-15 (resting NK cells) before proceeding to immunostaining. For NK cell-tumour co-cultures, freshly isolated NK cells were added to tumour cells cultured either as spheroids or monolayers for 24 hours.

Agarose-induced tumour spheroids.[43] A498 renal carcinoma cells were maintained in RPMI-1640 with L-glutamine (Sigma-Aldrich) supplemented with 10% FBS, 1x MEM Non-Essential Amino Acid Solution (Sigma-Aldrich) and 10 mM Hepes (Sigma-Aldrich). Molten 2% pure agarose (Sigma Aldrich) solution was poured onto the spheroid micro-mould (#12-256-Small, MicroTissues, Inc.) to obtain agarose hydrogels with 256 round-bottom micro-wells. Agarose micro-well hydrogels were transferred into a 24-well plate (Sigma Aldrich) and equilibrated in culture medium for 1 hour. A498 renal carcinoma cells were re-suspended at $1x10^6$ cells/mL and seeded in the agarose gel moulds (100 µL per gel). Cells were allowed to settle in the micro-wells for 30 min before 2 mL of culture medium was added. The agarose-induced spheroids were maintained in complete medium at 37 °C, 5% CO_2 for 24 hours before proceeding with NK co-culture.

NK cells and tumour spheroid co-culture. 100 µL of a suspension of $1x10^6$ cells/mL freshly isolated NK cells was transferred into the agarose gel moulds containing tumour (E:T ratio = 1:1), following the same procedure described above. IL-15 was added to the co-culture at a final concentration of 10 ng/mL. NK cells and tumour monolayer co-culture: A498 renal carcinoma cells and NK cells single cultures were obtained following the same procedure as agarose-induced spheroid cultures, in the absence of agarose hydrogels. Following 24 hours incubation, NK cells and tumour cells were collected to proceed with immunostaining. We defined extra-tumoral NK cells (oNKs) the fraction of NK cells residing in the co-culture supernatant, which we obtained by collecting the supernatant and washing the co-cultures twice. We defined intra-tumoral NK cells (iNKs) the NK cells residing within the tumour spheroids, which we obtained by dissociating the tumour spheroids with Accumax (Stemcell Technologies) for 45 minutes. The same treatment, including enzymatic dissociation, was performed on NK cell-tumour monolayer co-cultures. Accumax treatment was also performed on NK cells cultured alone and extra-tumoral NK cells, to avoid differences due to enzymatic treatment. NK cell interferon production and degranulation capability was assessed by performing a six-hour multiple response assay as previously described[55]. Briefly, NK cells were resuspended in complete medium (1 000 000 cells/mL), transferred in a V-bottom 96-well plates and co-cultured with K562 cells (ATCC) at 1:1 effector-to-target ratio in the presence of mouse anti-human CD107a Alexa Fluor 647 (BD Bioscience, clone H4A3, 2 uL/well) for 6 hours at 37°C. To block intracellular protein transport, BD GolgiStop (BD Bioscience) was added at a final concentration of 1:1000 during the assay after 1 hour of incubation. Once the 6 hours of incubation were completed, cells were washed twice in PBS + 2% FBS and stained with mouse anti-human CD45 Pe-Cy5 (BD Bioscience, clone HI30) and mouse anti-human CD107a Alexa Fluor 647 for 30 minutes at 4°C in the dark, followed by two washes in PBS and staining with fixable Viability Stain 510 (BD Bioscience, final concentration 1:1000) for 15 minutes at room temperature. Interferon gamma production was assessed by intracellular staining using mouse anti-human IFN-g FITC (BD Bioscience, clone 25723.11) and BD Cytofix/Cytoperm (BD Bioscience) following the manufacture's instructions. Cells were analyzed by flow cytometry using BD FACSCanto IVD 10, standard 3-lasers, 10 colors (BD Biosciences) and analyzed with the FlowJo Software v10 (FlowJO, LLC, RRID:SCR_008520).

Expansion of γδ T cells. Anonymous buffy coats from healthy donors were obtained from the department of Clinic Immunology and Transfusion medicine at Karolinska Hospital, Huddinge. PBMCs were isolated from buffy coat using a Ficoll-Paque Plus (Cytiva) gradient. γδ T cells were expanded from freshly prepared PBMCs for 14 days as follows: the PBMCs were cultured at $2x10^6$ cells/mL in AIM-V medium (ThermoFisher) supplemented with 10 % heat-inactivated human serum from human male AB plasma (Sigma-Aldrich), 2.5 µM zoledronic acid (Sigma-Aldrich) and 200 IU/mL of recombinant human IL-2 (PeproTech). The cells were re-stimulated with 100 IU/mL recombinant human IL-2 every 2 to 3 days.

Study Participants. The present study analysed PBMCs from 13 healthy donors, 13 Long COVID patients and 5 CLL patients. For healthy donors, cells were isolated either from anonymous Buffy Coats (7 donors) or blood samples (6 donors raging from ages 27 to 44 years). Long COVID patients were characterized with >12 weeks of objectively measurable organ damage/dysfunction following PCR-verified SARS-CoV-2 infection and not explained by the severity of acute COVID or treatments for the same. The analysis included 12 post-acute sequelae of COVID-19 (PASC) patients and 1 recovered PASC patients (PASC-R). Long COVID patients ranged from ages 35 to 64 years. Venous blood samples were collected at a single time point for each individual. Informed consent was obtained from all patients. The Swedish ethical permit is covered under Dnr 2021-03293. Samples from Chronic Lymphocytes Leukaemia (CLL) patients were collected after 3 months from the second dose of vaccination against COVID-19. patients were in their early-stage untreated CLL.

PBMCs isolation. PBMCs were isolated either from Buffy Coat (healthy donors) or blood (Long COVID and CLL patients) following a different protocol, depending on the sample. healthy donors and CLL patients: 45 mL of buffy coat was diluted 1:1 with PBS into 2x50 mL Falcon tubes and properly mixed. 30 mL of diluted solution was transferred in 2 new Falcon tubes pre-filled with 15 mL of Ficoll, using gravity-driven flow to overlay the diluted blood onto Filcoll. The tubes were centrifuged at 400 g for 25 minutes (brake off). The fraction containing PBMCs was collected into 2 new Falcon tubes and washed 2x with 45 mL PBS. During the washing steps, cells were pelleted by spinning the tubes at 300 g for 5 minutes (brake on). After the last washing, cells were resuspended in 20 mL PBS, filtered through a cell strainer, and pelleted one last time at 200 g for 10 minutes. After removal of the supernatant, cells were resuspended at a density of 10^8 cells/mL in a solution for cryopreservation (in 90% FBS + 10% DMSO) and stored in 1 mL batches at -140 ˚C until the analysis. *Long COVID patients:* Following plasma collection, blood was processed to isolate peripheral blood mononuclear cells (PBMCs) as follows: briefly, Lymphoprep™ (STEMCELL Technologies) was first added to SepMateTM tubes (STEMCELL Technologies) by carefully pipetting through the central hole of the SepMate insert, after which pre-diluted blood (Blood mixed with PBS + 2% FBS 1:1) was layered on the top of Lymphoprep™ (1 part of Lymphoprep : 2 parts of diluted blood) by pipetting it down the side of the tube carefully by minimizing the mixing of blood with Lymphoprep™ and centrifuged at 1200 x g for 10 minutes at ambient temperature (15 - 25°C) with the brake on. The top layer containing the enriched mononuclear cells (MNCs) was poured off into a new 50 mL tube and washed twice with PBS+2% FBS by centrifuging at 300 x g for 8 minutes at ambient temperature, with the brake on. Cells were then counted and cryopreserved (in 90% FBS + 10% DMSO) at a concentration of 5 million PBMCs/ml per cryotube stored at -80C first followed by transferring them to a liquid nitrogen tank for long-term storage.

Immune staining. Frozen PBMCs were thawed by adding a 10-fold volume of RPMI-1640 (Sigma-Aldrich) supplemented with 10% FBS (Sigma-Aldrich) and Benzonase Nuclease (10 units/mL, Sigma-Aldrich), pelleted at 400 g for 8 minutes, resuspended in 5 mL medium and kept 1 hour in the cell incubator for recovering.[56] For both cultured cells (*i.e.*, NK cells and γδ T cells) and isolated PBMCs in media, cells were pelleted at 400 g for 6 minutes and resuspended in Staining Buffer (eBioscience, ThermoFisher) at a concentration of $3x10^6$ cells/mL. Aliquots of 200 µL (*i.e.*, $6x10^5$ cells) in 0.5 mL Eppendorf were used to prepare single stained controls and multi-colour samples for flow cytometry. Optimal volumes of antibodies were obtained from calculation of staining indexes and each aliquot was stained with either single antibody (for single stained controls) or a cocktail of antibodies. For panels containing more than one Brilliant Violet (BV) dye, 30 µL of Brilliant Stain Buffer (ThermoFisher) was added to prevent dye aggregation. Cells were incubated at 4 ˚C in the darkness for 30 minutes, washed 2x with PBS (Gibco™, pH 7.4) and resuspended in 300 µL. Then, cells were stained

with 1 µL of Fixable Viability Stain 660 (BD Bioscience, stock solution: 5 ng/µL in DMSO) at room temperature for 15 minutes, washed 2x in PBS and resuspended to a final volume of 400 µL in the flow tubes. For each experiment, we built a different panel of fluorescent markers to gate on cells subpopulations, which was compatible with our probe for PM fluidity, namely Pro12A. *Panel for NK cells activation*: cells were stained with anti-Human CD3-BV605 (clone SK7, BD Biosciences) and CD56-APC-R700 (clone NCAM16.2, BD Biosciences). *Panel for NK cells activation*: cells were stained with anti-Human CD3-PE-Cy7 (clone SK7, BD Biosciences) and CD45-FITC (clone HI30, BioLegend). *Panel for γδ T cells expansion*: cells were stained with anti-Human CD3-BV605, CD27-BV711 (clone M-T271, BioLegend), Vγ9-FITC (clone B3, BioLegend), Vδ2-PE (clone B6, BioLegend), CD45RO-PE-Cy7 (clone UCHL1, BD Biosciences). *Panel for PBMCs from healthy donors and patients*: PBMCs were stained with anti-Human CD45-FITC, CD3-BV605, CD8-PE-FIRE700 (clone SK1, BioLegend), CD14-BV711 (clone M5E2, BioLegend), CD19-PE-Cy7 (clone SJ25C1, BioLegend), CD56-APC-R700, CD11c-PE (clone Bu15, BioLegend). PBMCs for microscopy measurements of monocytes were incubated with Alexa Fluor 647 anti-human CD14 (Biolegend) following the protocol described above and stained with Pro12A for GP quantification.

Analysis of PM fluidity. Cells (400 µL at a concentration = 1.5×10^6 cells/mL) were stained with 1.5 µL of Pro12A (100 µM in DMSO) and vortexed vigorously. After 1 minute from staining, we acquired flow data for ~5 minutes using a BD LSRFortessa 16-colour instrument. Before each experiment, we calibrated our flow pipeline by running DOPC-coated beads stained with Pro12A and adjusting the PMT voltages of the blue and green channels so to ensure the same median GP value for DOPC beads. Data from flow were analysed in FCS Express (DeNovo Software) and GP values from individual cells were normalized to the GP_{DOPC} to remove day-to-day variability.

UMAP analysis for clusters identification. Dimensionality reduction analysis was performed on live-$CD45^+$-gated cells using FCS express software. All fluorescent parameters (except ΔGP) were scaled using a biexponential transformation applying the fifth percentile method to calculate the Below Zero parameter. ΔGP values were scaled following a linear method. Cells were down sampled following the Interval Method or the Weighted Density Method for healthy donors and Long COVID patients or CLL patients, respectively. Sample size was kept at 10^6 cells and an alpha value of 25 and weight of 3 was chosen for the Weight Density down sampling. For UMAP analysis, we set number of neighbours equal to 50, Min Low Distance equal to 0.7 and number of iterations equal to 600.

Data availability

All data in this manuscript will be publicly available at FigShare repository upon publication.

Code availability

GP analysis from confocal microscopy images was performed using a customized algorithm in Python, which can be freely distributed upon request.

Acknowledgments

This work is supported by Swedish Research Council Starting Grant (grant no. 2020-02682), Wellcome Leap's Dynamic Resilience Program (jointly funded by Temasek Trust), SciLifeLab National COVID-19 Research Program financed by the Knut and Alice Wallenberg Foundation, Cancer Research KI, Human Frontier Science Program (RGP0025/2022) and Longevity Impetus Grant from Norn Group, Hevolution Foundation and Rosenkranz Foundation. We thank the SciLifeLab Advanced Light Microscopy facility and National Microscopy Infrastructure (VR-RFI 2016-00968) for their support on imaging.

Author contributions

L.A, E.S conceived and designed the experiments. L.A performed all the experiments together with Y.J and S.I (for experiment on PMBCs isolated from donors), P.S (for experiments on γδ T cells) and V.C (for experiments on NK cells). J.M and P.B. helped with collection of samples from Long Covid patients and provide scientific insights. M.B helped with collection of samples from CLL patients and provided scientific insights. P.S provided scientific insights on gamma delta T cells. B.O provided scientific insights on gamma delta and NK cells. A.S.K. provided Pro12A and insights on its use. L.A and E.S co-wrote the manuscript. All authors read and corrected the manuscript.

Competing interests

Authors declare no completing interest.

References

[1] Alexis J. Combes, Bushra Samad, and Matthew F. Krummel, "Defining and Using Immune Archetypes to Classify and Treat Cancer," *Nature Reviews Cancer* 23, no. 7 (July 2023): 491–505, https://doi.org/10.1038/s41568-023-00578-2.
[2] Adriana M. Mujal and Matthew F. Krummel, "Immunity as a Continuum of Archetypes," *Science* 364, no. 6435 (April 5, 2019): 28–29, https://doi.org/10.1126/science.aau8694.
[3] Caleb Lareau, "Subtle Cell States Resolved in Single-Cell Data," *Nature Biotechnology*, May 17, 2023, 1–2, https://doi.org/10.1038/s41587-023-01797-6.
[4] Gerrit van Meer, Dennis R. Voelker, and Gerald W. Feigenson, "Membrane Lipids: Where They Are and How They Behave," *Nature Reviews Molecular Cell Biology* 9, no. 2 (February 2008): 112–24, https://doi.org/10.1038/nrm2330.
[5] James A. Olzmann and Pedro Carvalho, "Dynamics and Functions of Lipid Droplets," *Nature Reviews Molecular Cell Biology* 20, no. 3 (March 2019): 137–55, https://doi.org/10.1038/s41580-018-0085-z.
[6] Bruce Alberts et al., "The Lipid Bilayer," in *Molecular Biology of the Cell. 4th Edition* (Garland Science, 2002), https://www.ncbi.nlm.nih.gov/books/NBK26871/.
[7] Doralicia Casares, Pablo V. Escribá, and Catalina Ana Rosselló, "Membrane Lipid Composition: Effect on Membrane and Organelle Structure, Function and Compartmentalization and Therapeutic Avenues," *International Journal of Molecular Sciences* 20, no. 9 (January 2019): 2167, https://doi.org/10.3390/ijms20092167.
[8] Matthias P. Wymann and Roger Schneiter, "Lipid Signalling in Disease," *Nature Reviews Molecular Cell Biology* 9, no. 2 (February 2008): 162–76, https://doi.org/10.1038/nrm2335.

[9] James C. Dodge, "Lipid Involvement in Neurodegenerative Diseases of the Motor System: Insights from Lysosomal Storage Diseases," *Frontiers in Molecular Neuroscience* 10 (2017), https://www.frontiersin.org/articles/10.3389/fnmol.2017.00356.
[10] Vijayakumar Natesan and Sung-Jin Kim, "Lipid Metabolism, Disorders and Therapeutic Drugs - Review," *Biomolecules & Therapeutics* 29, no. 6 (November 1, 2021): 596–604, https://doi.org/10.4062/biomolther.2021.122.
[11] Frances M. Platt et al., "Lysosomal Storage Diseases," *Nature Reviews Disease Primers* 4, no. 1 (October 1, 2018): 1–25, https://doi.org/10.1038/s41572-018-0025-4.
[12] Giancarlo Parenti, Diego L Medina, and Andrea Ballabio, "The Rapidly Evolving View of Lysosomal Storage Diseases," *EMBO Molecular Medicine* 13, no. 2 (February 5, 2021): e12836, https://doi.org/10.15252/emmm.202012836.
[13] Katie A. Wilson et al., "Understanding the Link between Lipid Diversity and the Biophysical Properties of the Neuronal Plasma Membrane," *Biochemistry* 59, no. 33 (August 25, 2020): 3010–18, https://doi.org/10.1021/acs.biochem.0c00524.
[14] J. H. Lorent et al., "Plasma Membranes Are Asymmetric in Lipid Unsaturation, Packing and Protein Shape," *Nature Chemical Biology* 16, no. 6 (June 1, 2020): 644–52, https://doi.org/10.1038/s41589-020-0529-6.
[15] G. Ekin Atilla-Gokcumen et al., "Dividing Cells Regulate Their Lipid Composition and Localization," *Cell* 156, no. 3 (January 30, 2014): 428–39, https://doi.org/10.1016/j.cell.2013.12.015.
[16] Govind Kunduri, Usha Acharya, and Jairaj K. Acharya, "Lipid Polarization during Cytokinesis," *Cells* 11, no. 24 (January 2022): 3977, https://doi.org/10.3390/cells11243977.
[17] Simone Braig et al., "Pharmacological Targeting of Membrane Rigidity: Implications on Cancer Cell Migration and Invasion," *New Journal of Physics* 17, no. 8 (August 2015): 083007, https://doi.org/10.1088/1367-2630/17/8/083007.
[18] V. Edmond et al., "Downregulation of Ceramide Synthase-6 during Epithelial-to-Mesenchymal Transition Reduces Plasma Membrane Fluidity and Cancer Cell Motility," *Oncogene* 34, no. 8 (February 19, 2015): 996–1005, https://doi.org/10.1038/onc.2014.55.
[19] Weina Zhao et al., "Candidate Antimetastasis Drugs Suppress the Metastatic Capacity of Breast Cancer Cells by Reducing Membrane Fluidity," *Cancer Research* 76, no. 7 (April 1, 2016): 2037–49, https://doi.org/10.1158/0008-5472.CAN-15-1970.
[20] Jennifer J. Lühr et al., "Maturation of Monocyte-Derived DCs Leads to Increased Cellular Stiffness, Higher Membrane Fluidity, and Changed Lipid Composition," *Frontiers in Immunology* 11 (2020): 590121, https://doi.org/10.3389/fimmu.2020.590121.
[21] Maria I. Matias et al., "Regulatory T Cell Differentiation Is Controlled by αKG-Induced Alterations in Mitochondrial Metabolism and Lipid Homeostasis," *Cell Reports* 37, no. 5 (November 2, 2021): 109911, https://doi.org/10.1016/j.celrep.2021.109911.
[22] Dylan M. Owen et al., "High Plasma Membrane Lipid Order Imaged at the Immunological Synapse Periphery in Live T Cells," *Molecular Membrane Biology* 27, no. 4–6 (August 1, 2010): 178–89, https://doi.org/10.3109/09687688.2010.495353.
[23] Carles Rentero et al., "Functional Implications of Plasma Membrane Condensation for T Cell Activation," *PLOS ONE* 3, no. 5 (May 28, 2008): e2262, https://doi.org/10.1371/journal.pone.0002262.
[24] Iztok Urbančič et al., "Aggregation and Mobility of Membrane Proteins Interplay with Local Lipid Order in the Plasma Membrane of T Cells," *FEBS Letters* 595, no. 16 (August 2021): 2127–46, https://doi.org/10.1002/1873-3468.14153.
[25] Maria Tello-Lafoz et al., "Cytotoxic Lymphocytes Target Characteristic Biophysical Vulnerabilities in Cancer," *Immunity* 54, no. 5 (May 11, 2021): 1037-1054.e7, https://doi.org/10.1016/j.immuni.2021.02.020.
[26] Jesse A. Rudd-Schmidt et al., "Lipid Order and Charge Protect Killer T Cells from Accidental Death," *Nature Communications* 10, no. 1 (November 27, 2019): 5396, https://doi.org/10.1038/s41467-019-13385-x.
[27] Yu Li and Jordan S. Orange, "Degranulation Enhances Presynaptic Membrane Packing, Which Protects NK Cells from Perforin-Mediated Autolysis," *PLOS Biology* 19, no. 8 (August 3, 2021): e3001328, https://doi.org/10.1371/journal.pbio.3001328.
[28] Richard K. P. Benninger et al., "Live Cell Linear Dichroism Imaging Reveals Extensive Membrane Ruffling within the Docking Structure of Natural Killer Cell Immune Synapses," *Biophysical Journal* 96, no. 2 (January 1, 2009): L13, https://doi.org/10.1016/j.bpj.2008.10.005.
[29] Abigail H. Pollock et al., "Prolonged Intake of Dietary Lipids Alters Membrane Structure and T Cell Responses in LDLr−/− Mice," *The Journal of Immunology* 196, no. 10 (May 15, 2016): 3993–4002, https://doi.org/10.4049/jimmunol.1501261.

[30] Fabio Zani et al., “The Dietary Sweetener Sucralose Is a Negative Modulator of T Cell-Mediated Responses,” *Nature* 615, no. 7953 (March 2023): 705–11, https://doi.org/10.1038/s41586-023-05801-6.
[31] Yosuke Niko and Andrey S Klymchenko, “Emerging Solvatochromic Push–Pull Dyes for Monitoring the Lipid Order of Biomembranes in Live Cells,” *The Journal of Biochemistry* 170, no. 2 (August 1, 2021): 163–74, https://doi.org/10.1093/jb/mvab078.
[32] Franziska Ragaller et al., “Dissecting the Mechanisms of Environment Sensitivity of Smart Probes for Quantitative Assessment of Membrane Properties,” *Open Biology* 12, no. 9 (September 14, 2022): 220175, https://doi.org/10.1098/rsob.220175.
[33] Mariana Amaro et al., “Laurdan and Di-4-ANEPPDHQ Probe Different Properties of the Membrane,” *Journal of Physics D* 50, no. 13 (April 5, 2017): 134004, https://doi.org/10.1088/1361-6463/aa5dbc.
[34] Andrey S. Klymchenko, “Fluorescent Probes for Lipid Membranes: From the Cell Surface to Organelles,” *Accounts of Chemical Research* 56, no. 1 (January 3, 2023): 1–12, https://doi.org/10.1021/acs.accounts.2c00586.
[35] José García-Calvo et al., “HydroFlipper Membrane Tension Probes: Imaging Membrane Hydration and Mechanical Compression Simultaneously in Living Cells,” *Chemical Science* 13, no. 7 (2022): 2086–93, https://doi.org/10.1039/D1SC05208J.
[36] Andrey S. Klymchenko, “Solvatochromic and Fluorogenic Dyes as Environment-Sensitive Probes: Design and Biological Applications,” *Accounts of Chemical Research* 50, no. 2 (February 21, 2017): 366–75, https://doi.org/10.1021/acs.accounts.6b00517.
[37] Dmytro I. Danylchuk et al., “Switchable Solvatochromic Probes for Live-Cell Super-Resolution Imaging of Plasma Membrane Organization,” *Angewandte Chemie International Edition* 58, no. 42 (2019): 14920–24, https://doi.org/10.1002/anie.201907690.
[38] Dmytro I. Danylchuk et al., “Redesigning Solvatochromic Probe Laurdan for Imaging Lipid Order Selectively in Cell Plasma Membranes,” *Analytical Chemistry* 92, no. 21 (November 3, 2020): 14798–805, https://doi.org/10.1021/acs.analchem.0c03559.
[39] Erdinc Sezgin et al., “Spectral Imaging to Measure Heterogeneity in Membrane Lipid Packing,” *ChemPhysChem* 16, no. 7 (2015): 1387–94, https://doi.org/10.1002/cphc.201402794.
[40] Witold K. Subczynski et al., “High Cholesterol/Low Cholesterol: Effects in Biological Membranes Review,” *Cell Biochemistry and Biophysics* 75, no. 3–4 (December 2017): 369–85, https://doi.org/10.1007/s12013-017-0792-7.
[41] Heming Ge et al., “Extracellular Matrix Stiffness: New Areas Affecting Cell Metabolism,” *Frontiers in Oncology* 11 (2021), https://www.frontiersin.org/articles/10.3389/fonc.2021.631991.
[42] Nicole M. Anderson and M. Celeste Simon, “The Tumor Microenvironment,” *Current Biology* 30, no. 16 (August 2020): R921–25, https://doi.org/10.1016/j.cub.2020.06.081.
[43] Hannah Prendeville and Lydia Lynch, “Diet, Lipids, and Antitumor Immunity,” *Cellular & Molecular Immunology* 19, no. 3 (March 2022): 432–44, https://doi.org/10.1038/s41423-021-00781-x.
[44] Valentina Carannante et al., “Chapter 12 - Generation of Tumor Spheroids in Microwells to Study NK Cell Cytotoxicity, Infiltration and Phenotype,” in *Methods in Cell Biology*, ed. Clément Thomas and Lorenzo Galluzzi, vol. 178, The Immunological Synapse – Part B (Academic Press, 2023), 195–208, https://doi.org/10.1016/bs.mcb.2023.01.001.
[45] Galit Alter, Jessica M. Malenfant, and Marcus Altfeld, “CD107a as a Functional Marker for the Identification of Natural Killer Cell Activity,” *Journal of Immunological Methods* 294, no. 1 (November 1, 2004): 15–22, https://doi.org/10.1016/j.jim.2004.08.008.
[46] Annelise Y. Mah and Megan A. Cooper, “Metabolic Regulation of Natural Killer Cell IFN-γ Production,” *Critical Reviews in Immunology* 36, no. 2 (2016): 131–47, https://doi.org/10.1615/CritRevImmunol.2016017387.
[47] Makoto Kondo et al., “Expansion of Human Peripheral Blood Γδ T Cells Using Zoledronate,” *JoVE (Journal of Visualized Experiments)*, no. 55 (September 9, 2011): e3182, https://doi.org/10.3791/3182.
[48] Kandice R. Levental et al., “Lipidomic and Biophysical Homeostasis of Mammalian Membranes Counteracts Dietary Lipid Perturbations to Maintain Cellular Fitness,” *Nature Communications* 11, no. 1 (March 12, 2020): 1339, https://doi.org/10.1038/s41467-020-15203-1.
[49] Dylan M. Owen et al., “Quantitative Imaging of Membrane Lipid Order in Cells and Organisms,” *Nature Protocols* 7, no. 1 (January 2012): 24–35, https://doi.org/10.1038/nprot.2011.419.
[50] Enrica Torretta et al., “Severity of COVID-19 Patients Predicted by Serum Sphingolipids Signature,” *International Journal of Molecular Sciences* 22, no. 19 (September 22, 2021): 10198, https://doi.org/10.3390/ijms221910198.

[51] Mojgan Masoodi et al., “Disturbed Lipid and Amino Acid Metabolisms in COVID-19 Patients,” *Journal of Molecular Medicine* 100, no. 4 (April 1, 2022): 555–68, https://doi.org/10.1007/s00109-022-02177-4.
[52] Alessandra Trojani et al., “Gene Expression Profiling Identifies ARSD as a New Marker of Disease Progression and the Sphingolipid Metabolism as a Potential Novel Metabolism in Chronic Lymphocytic Leukemia,” *Cancer Biomarkers: Section A of Disease Markers* 11, no. 1 (2012 2011): 15–28, https://doi.org/10.3233/CBM-2012-0259.
[53] Philipp Jung et al., “T Cell Stiffness Is Enhanced upon Formation of Immunological Synapse,” *eLife* 10 (July 27, 2021): e66643, https://doi.org/10.7554/eLife.66643.
[54] Miguel Paez-Perez and Marina K. Kuimova, “Molecular Rotors: Fluorescent Sensors for Microviscosity and Conformation of Biomolecules,” *Angewandte Chemie International Edition* n/a, no. n/a (n.d.): e202311233, https://doi.org/10.1002/anie.202311233.
[55] Yenan T. Bryceson et al., “Functional Analysis of Human NK Cells by Flow Cytometry,” *Methods in Molecular Biology (Clifton, N.J.)* 612 (2010): 335–52, https://doi.org/10.1007/978-1-60761-362-6_23.
[56] Bo Langhoff Hønge et al., “Optimizing Recovery of Frozen Human Peripheral Blood Mononuclear Cells for Flow Cytometry,” ed. Maria Cristina Vinci, *PLOS ONE* 12, no. 11 (November 1, 2017): e0187440, https://doi.org/10.1371/journal.pone.0187440.